

Spectral Densities from Dynamic Density-Matrix Renormalization

Carsten Raas* and Götz S. Uhrig†

Institut für Theoretische Physik, Universität zu Köln, Zùlpicher Str. 77, 50937 Köln, Germany†

(Dated: July 6, 2005)

Dynamic density-matrix renormalization provides valuable numerical information on dynamic correlations by computing convolutions of the corresponding spectral densities. Here we discuss and illustrate how and to which extent such data can be deconvolved to retrieve the wanted spectral densities. We advocate a nonlinear deconvolution scheme which minimizes the bias in the ansatz for the spectral density. The procedure is illustrated for the line shape and width of the Kondo peak (low energy feature) and for the line shape of the Hubbard satellites (high energy feature) of the single impurity Anderson model. It is found that the Hubbard satellites are strongly asymmetric.

PACS numbers: 71.55.Ak, 71.27.+a, 78.67.Hc, and 78.20.Bh

I. INTRODUCTION

The computation of spectral properties is a central issue in theoretical physics. Many spectroscopic probes provide experimental information about the investigated systems. In order to understand the meaning of such data it is indispensable to be able to compute the corresponding quantities theoretically. This task is particularly demanding if the system under study is characterized by strong correlations. Then standard approaches like diagrammatic perturbation theory have difficulties to provide quantitative results.

An archetypal class of strongly correlated systems are impurity models where a small subsystem, the impurity, is coupled to a bath of degrees of freedom. The discrete levels of the impurity are broadened due to the interaction with the bath. The most fundamental fermionic representative of this class of models is the single impurity Anderson model (SIAM)¹ where the impurity is characterized by a single fermion level which can be empty, or singly occupied with spin up or down, or doubly occupied. The energy of the doubly occupied state is increased by the interaction energy U . The bath is a bath of non-interacting fermions of either spin direction to which the impurity is coupled by hybridization. It is the aim of this article to present an algorithm to obtain the dynamics of a SIAM with high resolution on all energy scales.

The SIAM describes a plethora of physical problems. Historically it was used for diluted magnetic impurities in metals, see e.g. Ref. 1. But it also describes the electronic transmission through quantum dots, see e.g. Ref. 2. The smallness of the quantum dot implies a small capacitance, hence a large charging energy which represents the interaction energy U . The bath is given by the external leads. The dynamic mean-field theory (DMFT)^{3,4} represents another broad and very active field where the SIAM occurs. In this approach, as in all mean-field approaches, the lattice problem of strongly interacting fermions is mapped onto an effective single-site problem, namely a SIAM. This SIAM is linked to the original lattice problem by a self-consistency condition. The clue is that the mean-field, the Green function of the bath, is a dynamic quantity depending on frequency.

The above examples illustrate that it is very important to be able to compute the dynamics of a SIAM in a reliable fashion. There are several numerical approaches which can be applied. Among the most prominent ones are quantum Monte Carlo (QMC)⁵ and the numerical renormalization group (NRG)^{6,7}. Both approaches are powerful but do not have a high resolution away from the Fermi level. For QMC this is so since the dynamics is computed in imaginary time and the analytic continuation to real frequencies represents an ill-conditioned problem. Moreover, care must be taken to reach low temperatures. The NRG can be used directly at zero temperature. But it is set up to focus on the limit $\omega \rightarrow 0$. The energy levels kept are broadened by a broadening which is proportional to the frequency which implies that features at higher energies tend to be smeared out⁸.

We investigate here a third complementary numerical approach given by the dynamic density-matrix renormalization (D-DMRG)^{8,9,10,11,12,13,14}. Note that there is no complete consensus on the nomenclature. Jeckelmann uses the term ‘dynamic density-matrix renormalization group’ only for the approach using a variational principle¹³ while the approach used here is called correction vector density-matrix renormalization. We consider, however, ‘dynamic density-matrix renormalization group’ to be the general term for all algorithms computing dynamic correlations by DMRG in the frequency domain^{9,10,11,13} as opposed to DMRG approaches computing the dynamics in real time^{15,16} which efficiently implement ideas of Vidal^{17,18}. The approach used in this article determines the dynamics at zero temperature by computing the expectation values in the local propagator. This can be realized by targeting not only at the ground state and the excited state, but also at the resolvent applied to the excited state. This additional targeted state is called the correction vector.

The main limitation of the D-DMRG is that one cannot obtain data for purely real frequencies but only for frequencies with a certain imaginary part. Hence the extraction of the behavior at purely real frequencies is one of the main problems to be solved in using the D-DMRG^{8,14,19}. It is the main aim of the present paper to discuss and to compare various algorithms to achieve

this extraction. In particular, we will present a nonlinear approach from the family of maximum entropy methods. This approach provides a *continuous, positive* ansatz for the wanted spectral density with the *least bias* (LB).

In the following section II we will present the model and we will discuss the observable of interest. Next in Sect. III, we will discuss various extraction schemes, linear and non-linear ones. The features of these schemes will be illustrated by some toy spectral densities for which the broadened and the unbroadened data is analytically available. The results by the LB algorithm for the Kondo peak and the Hubbard satellites will be presented in Sects. IV and V, respectively. Finally, a short summary will be given in Sect. VI.

II. MODEL AND OBSERVABLE

We want to illustrate the above general remarks by D-DMRG calculations and the subsequent data analysis. As motivated in the introduction the single-impurity Anderson model (SIAM) at half-filling is a very good and interesting testing ground. We will focus on

$$\mathcal{H} = U \left(n_{d,\downarrow} - \frac{1}{2} \right) \left(n_{d,\uparrow} - \frac{1}{2} \right) + V \sum_{\sigma} \left(d_{\sigma}^{\dagger} c_{0,\sigma} + \text{h.c.} \right) + \sum_{n=0,\sigma}^{\infty} \gamma_{n+1} \left(c_{n,\sigma}^{\dagger} c_{n+1,\sigma} + \text{h.c.} \right) \quad (1)$$

with arbitrary symmetric density of states (DOS) $\rho_0(\omega)$ of the free ($U = 0$) one-particle Green function $G_0(\omega)$ of the d -electron. The d -electron represents the impurity which is correlated due to the interaction $U > 0$. The bath is represented by the coefficients $\gamma_n \geq 0$ in (1). They are the coefficients of the continued fraction of the hybridization function $\Gamma(\omega)$ (cf. Ref. 8). Any hybridization function with symmetric imaginary part $\rho_0(\omega) := -\pi^{-1} \text{Im} G_0(\omega + i0+)$ can be represented by an appropriate choice of the γ_n . Hence the representation of the bath as semi-infinite chain does not restrict the generality of the model.

The dynamics we wish to compute is the dynamics of the fermionic single-particle propagator of the d -electron. Aiming at the properties at $T = 0$ it reads

$$G(\omega + i\eta) = \left\langle 0 \left| d_{\sigma} \frac{1}{\omega + i\eta - (\mathcal{H} - E_0)} d_{\sigma}^{\dagger} \right| 0 \right\rangle + \left\langle 0 \left| d_{\sigma}^{\dagger} \frac{1}{\omega + i\eta + (\mathcal{H} - E_0)} d_{\sigma} \right| 0 \right\rangle. \quad (2)$$

Here the ground state is denoted by $|0\rangle$ and its energy by E_0 . Since we focus at a spin-disordered solution the propagator has no dependence on the spin index σ . Hence, it is not denoted as argument of G . The frequencies ω and η are real. The standard retarded Green function is obtained for $\eta \rightarrow 0+$

$$G_{\text{R}}(\omega) = \lim_{\eta \rightarrow 0+} G(\omega + i\eta). \quad (3)$$

The quantity we are looking for is the spectral density $\rho(\omega) := -\pi^{-1} \text{Im} G_{\text{R}}(\omega)$. If necessary the real part can be obtained from the Kramers-Kronig relation.

The D-DMRG provides data points at given values of $\omega = \xi_i$ for finite values of η_i

$$g_i = -\frac{1}{\pi} \text{Im} G(\xi_i + i\eta_i) = \frac{1}{\pi} \int_{-\infty}^{\infty} \frac{\eta_i \rho(\omega) d\omega}{(\xi_i - \omega)^2 + \eta_i^2}, \quad (4)$$

where we used the Hilbert representation in the second equation. No data can be obtained directly at $\eta = 0$ since the inversion of the Hamiltonian is singular and cannot be achieved numerically in a stable way. Henceforth, we will call data at finite values of η *raw* data. One way to extract the physically relevant data on the real axis is to look at a sequence of decreasing values of η in order to extrapolate the result¹⁴ to $\eta = 0$. This approach, however, is time-consuming and requires many resources, in particular, if one is interested in the whole spectral density. So the line followed in the present article is to use the raw data as input of a generalized scheme to extract the information on the spectral density $\rho(\omega)$.

III. EXTRACTION SCHEMES

We consider two classes of extraction schemes, linear ones and non-linear ones. Linearity means that there is a linear relation between the raw data and the wanted spectral density.

A. Linear Extraction Schemes

1. Deconvolution

If the unavoidable imaginary part η is constant for all frequencies Eq. (4) becomes

$$g_i = -\frac{1}{\pi} \text{Im} G(\xi_i + i\eta) = \frac{1}{\pi} \int_{-\infty}^{\infty} \frac{\eta \rho(\omega) d\omega}{(\xi_i - \omega)^2 + \eta^2} \quad (5)$$

so that the raw data is the convolution of the true spectral density $\rho(\omega)$ with the Lorentzian

$$L_{\eta}(\omega) = \frac{1}{\pi} \frac{\eta}{\omega^2 + \eta^2} \quad (6)$$

of width η . Hence the necessary step for retrieving $\rho(\omega)$ is a deconvolution. It can be achieved in various ways. One standard way is to deconvolve the raw data. This is done in the time domain reached by Fourier transform because the convolution in Eq. (5) becomes a product in the time domain

$$\rho(\tau)_{\text{raw}} = \exp(-\eta|\tau|) \rho(\tau), \quad (7)$$

where we use $\rho(\tau)$ for the Fourier transform of $\rho(\omega)$ and $\rho(\tau)_{\text{raw}}$ for the Fourier transform of the raw data. The

raw data $\{g_i\}$ is obtained in the first place as a discrete set. In order to obtain a quasi continuous distribution we interpolate the discrete set $\{g_i\}$ by splines²⁰ which leads to $\rho(\omega)_{\text{raw}}$. The Fourier transforms are most efficiently done by Fast Fourier algorithms²⁰. The actual deconvolution is done by dividing by $\exp(-\eta|\tau|)$ which inverts Eq. (7). Then one transforms back to the frequency domain. So this procedure is very efficient and straightforward⁸.

The restriction to be kept in mind is that splining and deconvolution cannot create information where no information was present before. If the input data is not precise enough or if the spline does not approximate the true continuous function $\rho(\omega)_{\text{raw}}$ well enough the deconvolution will fail to produce reasonable results. In practice this is seen in unreasonable values of $\rho(\tau)$ after the division by $\exp(-\eta|\tau|)$ because this division amplifies any inaccuracy for large values of $|\tau|$. This problem is circumvented by a suitable low-pass filter $p_{\tau_0, \Delta\tau}(\tau)$ which suppresses inaccurate values

$$\rho(\tau)_{\text{raw}} \exp(\eta|\tau|) \rightarrow \rho(\tau)_{\text{raw}} \exp(\eta|\tau|) p_{\tau_0, \Delta\tau}(\tau) \quad (8)$$

at large values of $|\tau|$ beyond τ_0 on the scale $\Delta\tau$. Of course, this implies that only a certain resolution in frequency can be achieved. In view of the inevitable inaccuracies of any numerical calculation one has to accept such a bound to the enhancement of the resolution. Nevertheless, the deconvolution enhances the resolution considerably and the final curve obtained is continuous for all practical purposes since the interpolation allows to make the grid as fine as needed.

The procedure is illustrated in Fig. 1 where we display a power law singularity $s(\omega) = \omega^{-\alpha}\Theta(\omega)$ exactly and convolved by a Lorentzian $L_\gamma(\omega)$ of width $\gamma = 0.05$

$$s(\omega; \gamma) = \frac{\cos[\pi(1-\alpha)/2 - \alpha \arctan(\omega/\gamma)]}{\sin(\pi\alpha) (\omega^2 + \gamma^2)^{\alpha/2}}. \quad (9)$$

This line shape is well known in photoelectron spectroscopy²¹, named the Doniach-Šunjić line shape²². Note that we changed the normalization so that (9) represents exactly the convolution of $\omega^{-\alpha}\Theta(\omega)$ with $L_\gamma(\omega)$. The raw data $g_i = s(\xi_i; \gamma = \eta)$ that we use for these curves is obtained analytically at $\xi_i = i * 0.05$ in the interval $\xi_i \in [-3, 5]$, see the curve with the circle symbols. We do not use real D-DMRG here since we want first to illustrate the extraction schemes under ideal circumstances. The effect of inaccuracies will be discussed below.

In judging the effect of the deconvolution one must keep in mind that the reconstruction of a diverging singular line is the worst case for any algorithm. We have chosen the Doniach-Šunjić line shape for illustration in order to highlight the differences in the various schemes. Below (Fig. 3) we will present results also for a smoother curve to show that such a curve can be reconstructed in a quantitatively reliable way.

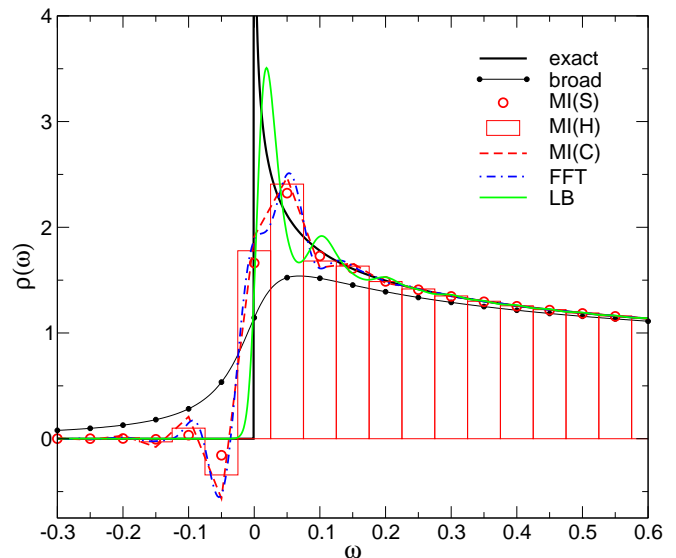


FIG. 1: Doniach-Šunjić line shape (Eq. (9)) for $\alpha = 1/4$ with (thin black solid line with circles representing the raw data at $\xi_i = 0.05i$) and without broadening (thick black solid line) $\gamma = \eta = 0.05$. The results of various schemes to retrieve the unbroadened line are shown: by deconvolution via fast Fourier transform (FFT), by matrix inversion assuming spikes (MI(S)) or histograms (MI(H)) or a piecewise linear continuous function (MI(C)), by the non-linear least-bias algorithm (LB). All schemes are described in the main text.

The dashed-dotted line is the result of the above described deconvolution using the low-pass filter

$$p_{\tau_0, \Delta\tau}(\tau) := \begin{cases} 1 & \text{for } |\tau| < \tau_0 - \Delta\tau \\ 0 & \text{for } |\tau| > \tau_0 + \Delta\tau \\ \left\{ 1 + \exp \left[\tan \left(\frac{\pi(|\tau| - \tau_0)}{2\Delta\tau} \right) \right] \right\}^{-1} & \text{otherwise} \end{cases} \quad (10)$$

which was also used to achieve the deconvolutions shown in Fig. 2 of Ref. 8. The parameter τ_0 determines where the low-pass cutoff is done; the parameter $\Delta\tau$ determines on which time-scale the cutoff function switches from 1 to 0. We used $\tau_0 \approx 10.7$ and $\Delta\tau \approx 0.763$. In practice, it turns out that it is fairly obvious in the τ -domain which values one has to choose for the low-pass filter. The data for too large values of $|\tau|$ scatter very much.

2. Matrix Inversion

A robust alternative to the deconvolution by Fourier transform is the explicit matrix inversion of the convolution procedure. This procedure shares the linearity with the Fourier transform and it may also lead to negative spectral weight close to abrupt changes of $\rho(\omega)$, for instance at singularities. An advantage over the Fourier deconvolution is that one may also consider variable widths η_i . In principle, this allows to adapt the grid $\{\xi_i\}$ to the

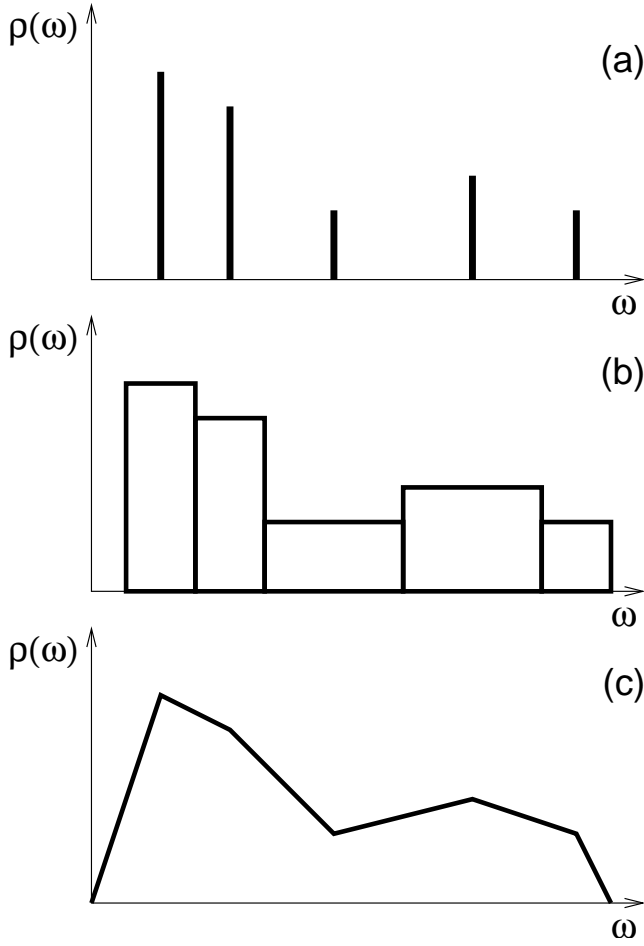


FIG. 2: Illustration of various assumptions on the behavior of the spectral density $\rho(\omega)$. (a) Spikes: $\rho(\omega)$ consists of a set of δ -functions with given positions, but unknown weights. (b) Histogram: $\rho(\omega)$ is piecewise constant with given positions of the jumps, but unknown heights ρ_i . (c) Continuous: $\rho(\omega)$ is piecewise linear and continuous with given positions of the cusps, but unknown values $\rho(\omega_i)$.

expected behavior of $\rho(\omega)$. A denser grid can be taken where the spectral density varies more rapidly.

The raw data $\{g_i\}$ provided by D-DMRG for a set of $\{\xi_i\}$ are taken as the components of the vector \mathbf{g} . Then the process of convolution can be described by a linear mapping \mathbf{M} of a set of linear parameters $\{l_i\}$ characterizing $\rho(\omega)$ onto the raw data $\{g_i\}$. Let us take the $\{l_i\}$ also as components of a vector \mathbf{l} . Then the convolution reads

$$\mathbf{g} = \mathbf{M} \mathbf{l}. \quad (11)$$

Clearly, the deconvolution implies the inversion of this equation. To this end, we have to choose the matrix \mathbf{M} to be square which means that there must be as many data values g_i as there are parameters l_i to be determined. It is obvious that this analysis is linear. The precise form of the matrix \mathbf{M} depends on further assumptions. Three

generic scenarios are studied; they are illustrated in Fig. 2.

a. Spikes Assuming that $\rho(\omega)$ is given as set of δ -functions (cf. Fig. 2a) with weights $\{w_i\}$ at given frequencies $\{\omega_i\}$. Then the weights constitute the linear parameters defining the spectral density. The matrix \mathbf{M} is derived from Eq. (4); it has simple matrix elements given by Lorentzians

$$M_{n,i} = L_{\eta_n}(\xi_n - \omega_i). \quad (12)$$

This approach has been proposed and used by Jeckelmann and coworkers^{14,19}. To have a square matrix problem the number of spikes has to equal the number of g_i determined by D-DMRG.

The rendering of the results is subtle. Since one cannot plot δ -functions they have to be broadened which adds another free parameter. Which broadening one has to choose is not *a priori* clear. For equidistant grids ω_i the distance between two consecutive peaks is a natural choice^{14,19}, cf. Fig. 1.

b. Histogram One assumes that $\rho(\omega)$ is piecewise constant $\rho(\omega) = \rho_i$ for $\omega_i < \omega \leq \omega_{i+1}$ (cf. Fig. 2b) where the frequencies ω_i are given beforehand. The set of linear parameters defining the spectral density are the values $l_i = \rho_i$. Again, Eq. (11) has to be solved. The matrix elements of \mathbf{M} are found from the integration of the right hand side of Eq. (4)

$$M_{n,i} = \pi^{-1} \arctan[(\omega - \xi_n)/\eta_n] \Big|_{\omega=\omega_i}^{\omega_{i+1}}. \quad (13)$$

The number of values ρ_i (not the number of ω_i) must be equal to the number of ξ_i to ensure that \mathbf{M} is square. The rendering is straightforward since the values ρ_i represent densities which can be plotted directly, cf. the histograms in Fig. 1.

c. Continuous One assumes that $\rho(\omega)$ is continuous and piecewise linear (cf. Fig. 2c) with $\rho(\omega_j) = \rho_j, j \in \{1, 2, 3, \dots, p\}$ at given frequencies ω_j . The values ρ_i represent the linear parameters $l_i = \rho_i$ which are determined by Eq. (11). The matrix elements result from the integration in Eq. (4). They are given by $M_{n,i} = \partial_{\rho_i} A_n(\xi_n)$ with

$$A_n(\xi) = \sum_{j=1}^{p-1} \left\{ \eta_n a_j \ln[\eta_n^2 + (\xi - \omega)^2]/(2\pi) + \right. \quad (14a)$$

$$\left. (\xi a_j + b_j) \arctan[(\omega - \xi)/\eta_n]/\pi \right\} \Big|_{\omega=\omega_j}^{\omega_{j+1}} \quad (14b)$$

$$a_j = (\rho_{j+1} - \rho_j)/(\omega_{j+1} - \omega_j) \quad (14b)$$

$$b_j = (\omega_{j+1}\rho_j - \omega_j\rho_{j+1})/(\omega_{j+1} - \omega_j). \quad (14c)$$

The number p must be equal to the number of raw data points. An example is depicted by the piecewise linear dashed curve in Fig. 1.

In all schemes, the numbers must be chosen such that \mathbf{M} is a square matrix. This is a necessary but not a sufficient condition for the existence of a unique solution \mathbf{l} in Eq. (11). In practice, we did not encounter problems in

the inversion of Eq. (11) as long as the raw data points were distributed rather evenly along the real axis. Only if there are data points accumulating in certain regions, for instance several data points at the same frequency, the inversion can be problematic. Loosely speaking this may occur since the raw data is slightly contradictory due to numerical inaccuracies. The broadening by the $\{\eta_n\}$ reduces the differences between the spectral densities. Hence small deviations in the raw data have large effects on the extracted spectral densities.

All linear extraction schemes do not guarantee that the extracted spectral density is non-negative, see Fig. 1. Whether this must be considered a serious drawback depends on the extent to which negative values occur and on the context in which the result is used. If the spectral density is the final result small regions of overshooting are unproblematic. If, however, the overshooting is considerable and if the spectral density shall be used in a subsequent step, e.g. in the self-consistency of a DMFT calculation, then negative values pose a severe problem. An important example is the determination of the coefficients of the continued fraction of the spectral density. This determination is only possible if the spectral density is really non-negative.

Another problem is the smoothness of the extracted density. Spurious discontinuities like the ones assumed in the spike ansatz or in the histogram ansatz (see Figs. 1 and 2) imply singularities in the real part of the propagator which is determined by the Kramers-Kronig relation. This in turn leads to unwanted features like slowly decaying oscillations in coefficients of the continued fraction. Of course, various schemes can be used to interpolate the discrete data provided by the matrix inversion approaches. But the interpolation represents an additional approximation which can be difficult to control.

B. Nonlinear Extraction Schemes

1. Basic Algorithm

In view of the drawbacks of the linear extraction schemes it is worthwhile to think about alternatives. The objective is to devise an ansatz for a continuous, non-negative spectral density $\rho(\omega)$ which is consistent with the numerically determined values of the raw data $\{g_i\}$ in Eq. (4). The ideal ansatz is completely unbiased. That means it does not use *any* information *other* than the one provided by the raw data. The information content of a density $\rho(\omega)$ is measured up to a constant by its negative entropy

$$-S = \int_{-\infty}^{\infty} \rho(\omega) \ln(\rho(\omega)) d\omega. \quad (15)$$

The least biased ansatz is the one with the least information content which is still compatible with the raw data. Hence we have to look for the density $\rho(\omega)$ which minimizes $-S$ (maximizes S) under the conditions (4) given

by the raw data $\{g_i\}$ and by the known normalization

$$1 = \int_{-\infty}^{\infty} \rho(\omega) d\omega. \quad (16)$$

To find this least biased ansatz (LB) is a straightforward task. Using the Lagrange multipliers $\{\lambda_i\}$ for the p conditions set by the raw data $\{g_i\}$ and the Lagrange multiplier $\tilde{\mu}$ for the normalization (16) the least biased ansatz is characterized by $\delta S = 0$, i.e.

$$0 = -1 - \ln(\rho(\omega)) + \sum_{i=1}^p \lambda_i L_{\eta_i}(\omega - \xi_i) + \tilde{\mu}. \quad (17)$$

This equation implies that the LB ansatz reads

$$\rho(\omega) = \exp \left[\mu + \sum_{i=1}^p \lambda_i L_{\eta_i}(\omega - \xi_i) \right], \quad (18)$$

where we defined $\mu = \tilde{\mu} - 1$. The Lagrange multipliers are determined by the nonlinear equations (16) and (4). They can be determined by any standard algorithm for a set of nonlinear equations. Via the ansatz (18), the $p + 1$ Lagrange multipliers determine the most unbiased spectral density $\rho(\omega)$ which is still compatible with the numerically measured information on $\rho(\omega)$.

The LB ansatz (18) is positive and continuous. Hence it avoids two major drawbacks of the linear extraction schemes. In spite of its continuity the LB ansatz is governed by a restricted number of parameters. Despite its positivity, the LB ansatz is able to reproduce rather abrupt changes in the spectral density, see Fig. 1. If arbitrarily accurate data at a fixed value of η were available on an arbitrarily dense grid, the LB algorithm were able to provide the correct result with arbitrary resolution (see also the discussion of Fig. 4 below). But the accuracy of the raw data required to achieve a certain resolution in the deconvolved result grows exponentially. So in practice this route cannot be followed very far and the broadening η sets the scale for the achievable resolution.

The least bias approach belongs to the class of maximum entropy methods (MaxEnt)²⁰. The main difference to standard MaxEnt is that we do not use a χ -functional in addition to the entropy function (15). The χ -functionals are bilinear in the density. They are introduced to account for possible deviations of the g_i from their true values. Such deviations occur for instance in quantum Monte Carlo calculations due to the inevitable statistical error. The D-DMRG data is free from statistical errors. Hence we can use the entropy functional alone as described above. The correction of numerical inaccuracies is discussed in more detail below.

We emphasize a major difference between the extraction of the spectral density $\rho(\omega)$ from D-DMRG data and from QMC. In the former case the task to be solved is to remove a small imaginary part $\omega + i\eta \rightarrow \omega$. This means that in the D-DMRG the raw data is situated slightly

above the real axis and has to be continued down to it. In the latter case the task to be solved is to continue QMC data from the imaginary axis (no real part) to the real axis $i\zeta \rightarrow \omega$. So the challenge in the QMC data analysis is much greater than in the D-DMRG data analysis. This explains why the D-DMRG approach is suited to investigate sharp features also at high energies⁸ while this is not a straightforward task by QMC.

The solution of the nonlinear equations (16) and (4) is done by a standard algorithm. There is no mathematical argument to show that there is only one unique solution. For instance, we found that the normalization of the spectral density need not be ensured by the parameter μ . This parameter can be fixed to almost any value. The remaining Lagrange parameters suffice to determine good approximations to $\rho(\omega)$ which fulfill the normalization condition (16) well. This implies that iterative numerical solutions have difficulties to fix μ independently. The root-finder algorithms run much more stable if the normalization is not included in the set of equations. Yet the resulting densities are normalized if the raw data provides a reasonable scan of the spectral density, i.e. if there is raw data at all frequencies ω where the density is non-negligible.

For other sum rules, for instance the second moment $\langle \omega^2 \rangle$, the same conclusion holds. If the raw data scans all relevant frequencies the sum rules do not provide useful additional information. But if raw data is only available for restricted frequency intervals, the sum rules help to improve the LB ansatz.

Furthermore, the iterative numerical solutions depend sometimes on the initial values. But the resulting $\rho(\omega)$ are in general (almost) identical. This remains true if the iterative algorithm does not find a true solution of the set of non-linear equations but only a set of parameters which makes the deviations

$$\Delta g_i := g_i - \frac{1}{\pi} \int_{-\infty}^{\infty} \frac{\eta_i \rho(\omega) d\omega}{(\xi_i - \omega)^2 + \eta_i^2} \quad (19)$$

small but fails to make them zero. In summary, the iterative determination of the Lagrange multipliers does not represent a major problem.

In Fig. 1 we display a comparison of all data extraction schemes introduced so far. The line shape to be found is a singular power law divergence. This line shape constitutes an unsolvable task since a divergence cannot be reproduced by the algorithms discussed. But this example illustrates well to which extent the algorithms manage to render the true distribution of spectral weight. All the linear schemes lead to regions of negative spectral densities which is a severe drawback. The divergence is approximated by a broad peak located at 0.05 away from the position of the divergence. There are some spurious oscillations in the approximated spectral density.

The LB scheme avoids negative spectral weight by construction. The divergence is approximated by a sharper peak at about 0.02 away from the position of the divergence. The algorithm implies spurious oscillations in the

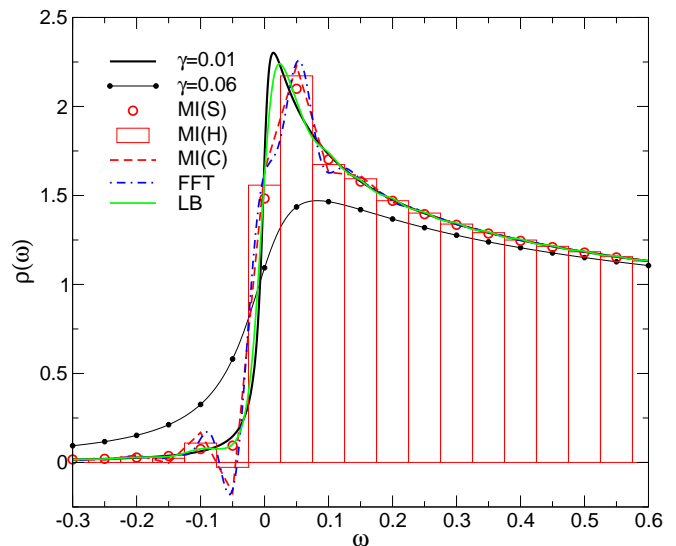


FIG. 3: Exact (thick black solid line) and broadened (by $\eta = 0.05$, thin black solid line with circles representing the raw data at $\xi_i = 0.05i$) lines derived from the Doniach-Sunjić line shape in Eq. (9), see also main text. The results of various schemes to retrieve the unbroadened line are shown: by deconvolution via fast Fourier transform (FFT), by matrix inversion assuming spikes (MI(S)) or histograms (MI(H)) or a piecewise linear continuous function (MI(C)), by the non-linear least-bias algorithm (LB).

approximated spectral density. So we conclude that the LB analysis represents a very efficient reconstruction of the unbroadened data even though the spurious oscillations can be a nuisance.

On the other hand it is, of course, possible to improve the analysis. An additional data point at $\omega \approx 0.02$ will certainly help all algorithms to reproduce the unbroadened density more faithfully. The same is trivially true for a denser mesh of raw data points. The former solution, however, requires either to intervene manually in the data analysis or to know beforehand where the peaks will be located. The latter requires much more numerical effort on the D-DMRG level so that this is not the most efficient approach.

In Fig. 3 we present the analysis of a smooth exact curve, namely the line shape in (9) at $\gamma = 0.01$. The curve broadened by $\eta = 0.05$ is the one at $\gamma = 0.06$ since the widths of Lorentzians is additive under convolution, in contrast to the root-mean-square of narrower distribution functions. Clearly, the extraction schemes do a better job for this non-singular case. The regions of negative spectral density in the linear schemes has shrunk. The LB scheme manages to reproduce the true density almost perfectly. The spurious oscillations are negligible. If we had chosen $\gamma = 0.02$ for the exact curve the LB density would be hardly distinguishable from the exact curve.

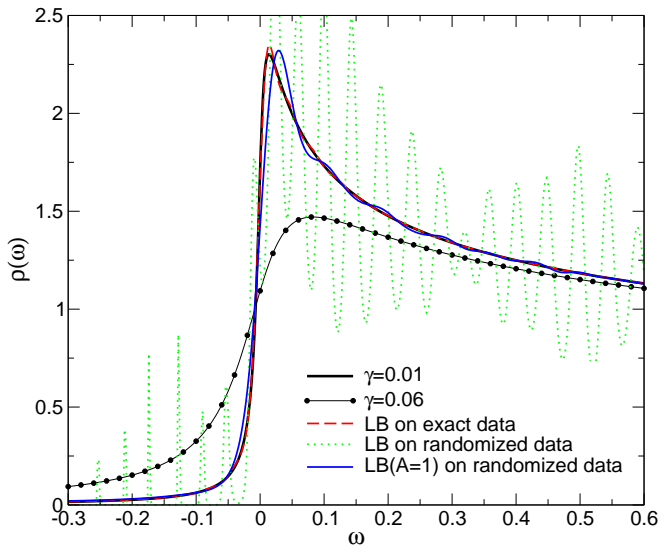


FIG. 4: Exact (thick black solid line) and broadened (by $\eta = 0.05$, thin black solid line with circles representing the raw data at $\xi_i = 0.02i$) lines derived from the Doniach-Sunjić line shape in Eq. (9). The dashed line depicts the density extracted from exact raw data by the LB scheme (the curve lies on top of the thick black line except at the maximum). The dotted oscillations are the LB result from data contaminated by a random error, see main text. The thin solid line represents the density derived from the contaminated data by the robust LB scheme with $A = 1$ using Eqs. (21,22).

2. Robustness towards Inaccuracies

So far we analyzed ideal raw data, i.e. no errors were considered. Statistical errors do not occur in the D-DMRG approach but systematic errors occur. There are two main sources for such errors. The first is the inaccuracy of the algorithm due to the truncation of the Hilbert space. This is an unavoidable error; but it can be controlled by comparing the results for different numbers of states kept in the density-matrix renormalization. We perform our calculations for 128 and for 256 states using the representation of spinful fermions as two kinds of spins via a double Jordan-Wigner transformation⁸. The relative truncation error in the spectral densities is estimated to be of the order of 10^{-5} to 10^{-3} depending on the frequency where it is computed. For low values of the frequency ($|\omega| \lesssim D$ in our model) the lower error applies; for frequencies beyond D the larger value applies.

The second important source of inaccuracy are finite-size effects. In principle, we wish to compute the spectral density for the infinite system. But this is not feasible numerically. So the system – the infinite chain – is approximated by finite chains of $L = 120$ to 400 sites. In a rigorous sense, the spectral density of the finite system consists of δ -functions, i.e. it is not a continuous function. But we do not intend to resolve all the fine details of the finite system. Rather we interpret our numerical

raw data obtained for the finite chain as an approximate description of the infinite system. The deviation of the raw data for the finite chain from the desired raw data of the infinite chain is considered the source of a systematic error, the finite-size effect. There are two conceivable ways to deal with this error. One way is to perform an extrapolation in system size L for each raw data point g_i before the deconvolution is done. The other way is to deconvolve the raw data for various chain lengths and to check whether the results still depend on the length L .

In our work, we have chosen the second approach because the first is hampered by an unsystematic behavior of g_i on L . Depending on details a particular δ -peak of the finite systems contributes more or less to the g_i under study. This makes a controlled extrapolation for all $\{g_i\}$ difficult, if not impossible.

In the second approach, care must be taken that the length L is so large that the raw data is sufficiently close to the raw data of the infinite system. In practice, this puts a restriction on η and L , see Sect. IV and Ref. 13. Of course, the use of finite chains restricts the extent to which we may extract information on the exact infinite system from the broadened data obtained for the finite system.

Another sort of errors are rounding errors. But they are of minor importance compared to the two other sources discussed above.

In Fig. 4 we display the LB analysis of raw data for the exact curve at $\gamma = 0.01$. In contrast to the procedure in Fig. 3 we use a finer grid of $\xi_i = i * 0.02$ for the raw data (curve with circles). The extracted curve represents the exact one very well, see the dashed line in Fig. 4. The agreement is significantly better than the one reached in Fig. 3. This illustrates that sufficiently accurate broadened data at fixed η can be used to resolve features of widths below η .

As explained above, there are in practice restrictions to better resolutions due to the systematic errors, namely the truncation of the basis and the finite-size effect. To examine the effect of systematic errors on the LB deconvolution we deliberately contaminated the raw data by an error of the order of 10^{-3} according to

$$g_i \rightarrow g_i * (1 + 10^{-3}x) \quad (20)$$

where x is a random number between -1 and 1 . The randomness is just used to mimic a systematic error which is uncorrelated from frequency to frequency. We obtained qualitatively very much the same results for a non-random error $g_i \rightarrow g_i * (1 + 10^{-3} \cos(\sqrt{5}i))$.

If the data is slightly inaccurate the deconvolution indeed fails as illustrated by the wild oscillations of the dotted line. We conclude that the occurrence of strong oscillations can be taken as criterion that the used raw data is not accurate enough for the LB analysis, i.e. the systematic errors are too large.

The thinner solid line depicts a successful deconvolution of the contaminated raw data. It is achieved by a

modification of the LB algorithm which makes it a standard maximum entropy approach. The negative entropy functional (15) is supplemented as shown

$$F[\rho(\omega)] := -S[\rho(\omega)] + A\chi[\rho(\omega)] \quad (21)$$

$$= \int_{-\infty}^{\infty} \rho(\omega) \ln(\rho(\omega)) d\omega + A \sum_i (\Delta g_i)^2$$

by a quadratic functional χ which measures the distance from the perfect fulfillment of the conditions (4). The differences Δg_i are defined in Eq. (19). The minimization of the functional F leads to the same ansatz (18) as before except that the parameters λ_i are now given by

$$\lambda_i = 2A\Delta g_i. \quad (22)$$

The set of these nonlinear equations (instead of $\Delta g_i = 0$ as for the pure LB approach) is used to determine the parameters λ_i . It is obvious that the robust modification of the LB ansatz becomes the pure LB ansatz in the limit of $A \rightarrow \infty$ since in this limit the deviations Δg_i vanish for given values of the Lagrange parameters λ_i . If the data is only weakly contaminated by inaccuracies, large values of A can be used to extract the spectral densities. Our example in Fig. 4 shows fairly strongly perturbed data. Still the robust LB can make sense out of them and retrieves a good approximation to the underlying curve.

The modified LB ansatz (21) is more robust since it can deal with some inaccuracies or inconsistencies of the raw data. Imagine that we deal with raw data on a fine grid where the distance between the data points is significantly smaller than the Lorentzian width $\eta_i \gg (\xi_{i+1} - \xi_i)$. Then g_{i+1} and g_i may differ only slightly if they are derived from a smooth continuous density $\rho(\omega)$. Any inaccuracy spoils this relation and may introduce significant spurious oscillations, see Fig. 4. As we stressed already previously the broadening makes different data more alike. Hence, the inverse process enhances slight differences like the ones between exact and inaccurate raw data greatly. The robust LB ansatz (21) helps to make the data extraction less sensitive to such effects without losing much resolution. Thereby, spurious oscillations can be suppressed.

The robust LB scheme opens the possibility to resolve features of widths below a given value of the broadening η by using a finer grid with $\Delta\xi < \eta$ since slightly inaccurate data can still be deconvolved. In this way, one may avoid the explicit use of small values of η . We emphasize, however, that the data must be accurate enough to contain the information on the relevant physics. Of course, the robust LB approach is no means to extract information which is not given by the raw data. For instance, one may stick to short chain lengths *only* if the underlying physical problem does not demand to describe long-range spatial fluctuations.

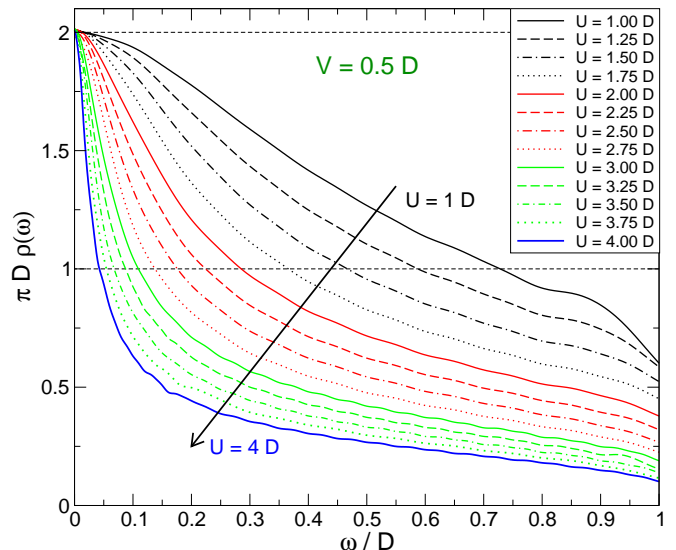


FIG. 5: Kondo peaks for the single-impurity Anderson model (1) for a hybridization function with semi-elliptic spectral density and $V = D/2$. On increasing interaction the Kondo peak becomes rapidly narrower.

IV. KONDO RESONANCE

Next we present data for the local spectral density $\rho(\omega)$ for the SIAM as introduced in Sect. II. In the present section we focus on the behavior at low energies where $\rho(\omega)$ is dominated by the Kondo peak, see e.g. Ref. 1. This peak can be computed by NRG in a very efficient way^{1,6,7}. So the idea of the present calculation is not to provide novel data, but to gauge the D-DMRG and to demonstrate that features at low energies can be resolved. We use the LB scheme to extract the real spectral density from the raw data as explained above. This is one of the differences to the investigation by Nishimoto and Jeckelmann¹⁴. For details of the numerical realizations we refer to previous works^{8,14}. Another difference concerns the parameter regime. We consider here interaction values U beyond the bare band width $W = 2D$, i.e. $U > 2D$, while Nishimoto and Jeckelmann look at Lorentzian bare spectral function whose band width is very large. But for the low energy region this difference is only a quantitative one.

Our results are depicted in Fig. 5. We have chosen the parameters such that the hybridization function has a semi-elliptic spectral density. The hybridization is taken to be $V = D/2$ so that the spectral density of the d -site without interaction is semi-elliptic, too. Clearly visible is the rapid narrowing of the Kondo peak on increasing interaction. Note that the density at zero energy $\rho(0)$ is pinned to its non-interacting value as required by the sum rules^{1,23,24,25}. This exact result is fulfilled to numerical accuracy which ranges from 0.1% for smaller interactions to 1% at larger interactions, see Fig. 5.

The data in Fig. 5 is obtained on various grids in fre-

quency, for various chain lengths and for varying widths η . All calculations are done with $m = 128$ sites kept in the truncations of the DMRG. The chain lengths L vary between 120 and 400 fermionic sites which translates to 240 (e.g. at $U = 1.25D$) to 800 (e.g. at $U = 4.00D$) spin sites after the double Jordan-Wigner transformation. The smaller the widths η are chosen the longer the chains have to be taken^{12,13}. A chain of L fermionic sites implies L main peaks distributed over the band width $W = 2D$. Assuming a roughly equidistant distribution the distance between two main peaks is W/L which should be significantly smaller than η

$$2W/L \leq \eta \quad (23)$$

in order to ensure that the discrete structure of the finite system is sufficiently smeared out. Then the data provided can be interpreted reasonably well as data of the infinite system.

Since the calculations are less costly at low energies than at higher energies we used mixed raw data coming from various chain lengths. The width η is varied correspondingly; we always used $\Delta\xi = \xi_{i+1} - \xi_i = \eta$. For instance at $U = 4D$, we used $L = 400$ with $\eta = 0.01D$ between $\omega = 0.00$ and 0.05 ; $L = 200$ with $\eta = 0.02D$ between $\omega = 0.06$ and 0.18 ; $L = 200$ with $\eta = 0.05D$ between $\omega = 0.20$ and 2.95 ; $L = 120$ with $\eta = 0.10D$ between $\omega = 3.00$ and 4.00 . The analysis of the raw data was done in all cases by the pure LB ansatz (18) with the conditions $\Delta g_i = 0$. There was no need to use the robust LB with $\lambda_i = 2A\Delta g_i$.

The rapidly narrowing peaks in Fig. 5 are characterized by the Kondo energy scale T_K . This scale can be read off from the spectral densities, for instance as half the width at half the maximum, i.e. at $\pi D\rho(\omega = T_K) = 1$. From analytic considerations¹, it is known that the Kondo energy scale is exponentially small in the interaction

$$T_K \propto V\sqrt{D/U} \exp(-\pi UD/(4V)^2). \quad (24)$$

This formula applies in the limit of $U \gtrsim W = 2D$ which is called the Schrieffer-Wolff limit of the SIAM. It holds for $U \rightarrow \infty$. The numerical results for the Kondo scale and the analytical prediction (24) agree very well in Fig. 6. Only for $U < W$ deviations occur as was to be expected. The widths at large values of U ($U > 4D$) are found from results for $\rho(\omega)$ where we extracted only the behavior at low energies. To determine the HWHM it is not necessary to know the whole line shape. It is an asset of the LB extraction scheme that it allows also to determine only a part of the whole curve. In conclusion, Fig. 6 demonstrates that the dynamic DMRG is able to reproduce the low energy scale of the SIAM over two orders of magnitude.

V. HUBBARD SATELLITES

In this section we show that the D-DMRG combined with the powerful LB scheme allows to resolve features

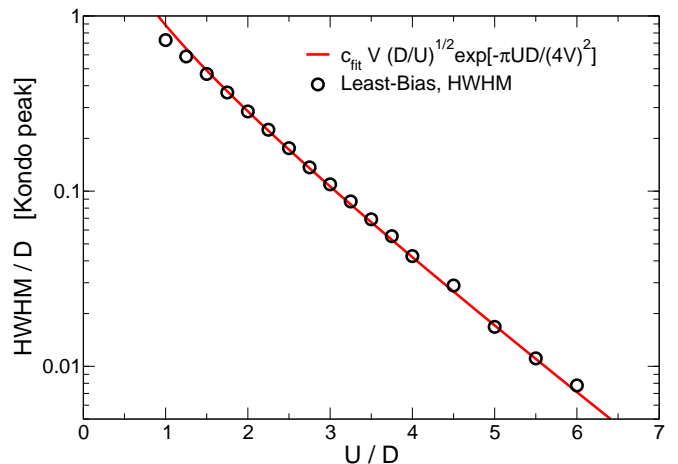


FIG. 6: Kondo energy scale (Kondo temperature) for the single-impurity Anderson model (1) for a hybridization function with semi-elliptic spectral density and $V = D/2$ in the Schrieffer-Wolff limit $U > 2D$. Symbols: half-width-half-maximum (HWHM) read off from $\rho(\omega)$ as found by the LB analysis of D-DMRG raw data; line: analytic result in Eq. 24. The proportionality factor of the fit is $c_{\text{fit}} = 3.887$.

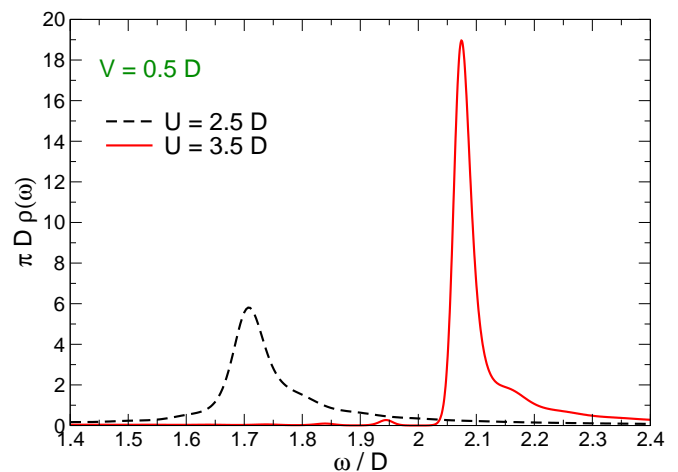


FIG. 7: Upper Hubbard satellite for two values of the interaction U obtained from D-DMRG raw data ($\eta = 0.1D$, $\Delta\xi = 0.05D$, $m = 256$, $L = 120$) processed by the LB scheme. At larger U a strongly asymmetric line shape occurs.

at high energies which so far eluded a quantitative determination. The calculation of the line shapes of energy levels at high energies represents a new field of applications since previous methods are not suited to perform such computations. An exception are features at high energies which can be understood and described as shifted low energy features²⁶. We emphasize that the progress in the manipulation of quantum dots by optical means has brought the measurements of high energy features within reach, see e.g. Refs. 27 and 28.

In a previous work⁸, we have shown that the Hubbard

satellites at about $\omega = \pm U/2$ become increasingly sharp once the interaction U is larger than the bandwidth $W = 2D$. In that work, however, we were not able to resolve the sharp Hubbard satellites since the deconvolution by Fourier transform was not powerful enough to do so, cf. Sect. III. By means of the LB extraction we are now able to address the line shape. In Fig. 7 the results for a moderate value of U ($2.5D$) and for a larger value of U ($3.5D$) are shown. While the line at $U = 2.5D$ is still fairly symmetric (cf. also the line for $U = 2D$ in Fig. 2 of Ref. 8) the line at $U = 3.5D$ has a clear asymmetric shape. The rise at the low energy side is rather abrupt and steep while the decrease at the high energy side is much more gentle and slow. The peak is very pronounced and the maximum value very high. The small bumps left of the peak are artefacts of the data extraction similar to the small dip in front of the uprise in Fig. 3. We also consider the shoulder on the right side of the peak in Fig. 7 to be an artefact of the data analysis in analogy to the spurious oscillations in Fig. 1.

At present, we do not have an analytical description of the line shape in Fig. 7. Qualitatively, however, the following description holds. The doubly occupied level has the energy $U/2$ in the atomic limit for $V = 0$. This level is shifted to higher energies by a finite hybridization $V > 0$ ^{8,29} and it is broadened⁸. The shift $\propto V^2/U$ is due to level repulsion between the doubly occupied level and modes where the doubly occupied level excites additional particle-hole pairs. A rough, averaged description of the broadening is provided by Fermi's golden rule implying that the width is proportional to V^4/U^2 .

In view of the asymmetric line shape and of the very narrow peak this averaged picture can be improved. The narrow peak itself has a certain intrinsic width which is small. Note that the general understanding of the SIAM as a local Fermi liquid implies that there are no singularities in the propagator. The spectral density is a smooth function, though it may display very narrow features. This is in contrast to the X-ray edge problem where the added fermion is completely immobile (no recoil).

The intrinsic width of the narrow peak results from the decay of the doubly occupied level into particle-hole pairs of the local Fermi liquid. According to Fermi's golden rule such a decay can take place only if the energy of the initial and the final state is equal which means that many particle-hole pairs have to be excited in order to make up for the relatively large energy $\approx U/2$ of the double occupancy. Very many particle-hole pairs are needed in view of the reduced effective band width of the order of the Kondo energy scale T_K . This argument accounts for a finite, though very large, life time of the doubly occupied level as seen in Fig. 7.

The high energy tail of the line in Fig. 7 can be understood as an effect of particle-hole pairs which are generated by the double occupancy. This is *not* the same as the decay of the double occupancy described above. In the decay the double occupancy disappears in the process while it remains on generating additional particle-

hole pairs. This explains why the contribution of this process is found at the high energy side of the peak in Fig. 7. The additional particle-hole pairs require an additional amount of energy to be created. The physics of this process is similar to the physics of the X-ray edge problem where the change of a local potential induces infinitely many particle-hole pairs thus leading to slowly decreasing tails in the spectra, see for instance Ref. 30 and references therein. The main difference to the X-ray edge problem is that there is no true singularity here so that the line shape is smoother.

At present, the accuracy of the data in the high energy tails is not sufficient to search for approximate power laws which possibly describe the tails of the Hubbard satellites in Fig. 7.

VI. SUMMARY

In this article, we discussed a variety of schemes to extract the spectral density $\rho(\omega)$ from the results of dynamic density-matrix renormalization data. All these schemes have the aim to remove the unavoidable broadening which has to be included in a D-DMRG calculation. The linear schemes use either Fourier transform to deconvolve the raw data or they implement an explicit matrix inversion. These schemes are linear because there is a linear relationship between the raw data and the extracted spectral density. If the structures to be resolved are not too sharp the linear schemes work well. If there are sharp structures the linear schemes are prone to lead to negative spectral densities which result from spurious oscillations. Furthermore, they can resolve the positions of sharp peaks only with the accuracy of the grid on which the raw data has been computed.

The nonlinear scheme introduced belongs to the family of maximum entropy methods. If the raw data is sufficiently accurate the least-bias approach works very well. It provides a positive and continuous ansatz for the spectral density with the least possible bias. Even relative abrupt changes of the spectral density can be reproduced satisfactorily. In the vicinity of singularities spurious oscillations occur. But they do not violate the positivity of the ansatz. The least-bias ansatz can be made more robust towards small numerical inaccuracies and finite-size effects by including besides the entropy functional a χ -functional in the functional to be minimized. Thereby, one can allow for small deviations from the raw data.

The properties of the above mentioned schemes were illustrated by calculations for a singular toy spectral density of the Doniach-Šunjić type. D-DMRG calculations were carried out and presented for the Kondo energy scale of the symmetric single impurity Anderson model in the Schrieffer-Wolff limit of $U > W$ where U is the interaction and W the band width. The Kondo energy scale could be retrieved over two orders of magnitude.

The reproduction of the Kondo energy scale served as a gauge for the approach. To our knowledge, numerically

exact results like those obtained for the line shape of the Hubbard satellites at $\omega = \pm U/2$ beyond the region of the bare band $\omega \in [-D, D]$ are not available in the literature. By these line shapes we extended our previous analysis of the Hubbard satellites⁸. Furthermore, these line shapes illustrate that the dynamic density-matrix renormalization is suited to provide high resolution data at high energies, i.e. away from the Fermi level. It is to be expected that such information will become more and more important as the experimental techniques are improving.

Acknowledgments

We thank T. Costi, R. Helmes, F. Gebhard, Y. Kuramoto, E. Müller-Hartmann, A. Rosch and L. H. Tjeng for helpful discussions and the DFG for financial support in SFB 608.

-
- * *Electronic address:* raas@lusi.uni-sb.de
† *Electronic address:* uhrig@lusi.uni-sb.de;
Homepage: <http://www.uni-saarland.de/fak7/uhrig/>
‡ *Present address:* Theoretische Physik FR 7.1, Gebäude 38, Universität des Saarlandes, 66123 Saarbrücken, Germany
- ¹ A. C. Hewson, *The Kondo Problem to Heavy Fermions* (Cambridge University Press, Cambridge, 1993).
 - ² M. Pustilnik and L. Glazman, J. Phys.: Condens. Matter **16**, R513 (2004).
 - ³ T. Pruschke, M. Jarrell, and J. K. Freericks, Adv. Phys. **44**, 187 (1995).
 - ⁴ A. Georges, G. Kotliar, W. Krauth, and M. J. Rozenberg, Rev. Mod. Phys. **68**, 13 (1996).
 - ⁵ J. E. Hirsch and R. M. Fye, Phys. Rev. Lett. **56**, 2521 (1986).
 - ⁶ O. Sakai, Y. Shimizu, and T. Kasuya, J. Phys. Soc. Jpn. **58**, 3666 (1989).
 - ⁷ T. A. Costi and A. C. Hewson, Physica B **163**, 179 (1990).
 - ⁸ C. Raas, G. S. Uhrig, and F. B. Anders, Phys. Rev. B **69**, 041102(R) (2004).
 - ⁹ K. A. Hallberg, Phys. Rev. B **52**, 9827 (1995).
 - ¹⁰ S. Ramasesha *et al.*, Synthetic Metals **85**, 1019 (1997).
 - ¹¹ T. D. Kühner and S. R. White, Phys. Rev. B **60**, 335 (1999).
 - ¹² T. Hövelborn, *Boundary Dynamics of the XY Chain by Density-Matrix Renormalization Group* (Diplomarbeit; available at <http://www.uni-saarland.de/fak7/uhrig/>, Bonn/Köln, 2000).
 - ¹³ E. Jeckelmann, Phys. Rev. B **66**, 045114 (2002).
 - ¹⁴ S. Nishimoto and E. Jeckelmann, J. Phys.: Condens. Matter **16**, 613 (2004).
 - ¹⁵ S. R. White and A. E. Feiguin, Phys. Rev. Lett. **93**, 076401 (2004).
 - ¹⁶ A. J. Daley, C. Kollath, U. Schollwöck, and G. Vidal, J. Stat. Mech.: Theor. Exp. P04005 (2004).
 - ¹⁷ G. Vidal, Phys. Rev. Lett. **91**, 147902 (2003).
 - ¹⁸ G. Vidal, Phys. Rev. Lett. **93**, 040502 (2004).
 - ¹⁹ F. Gebhard *et al.*, Eur. Phys. J. B **36**, 491 (2003).
 - ²⁰ W. H. Press, S. A. Teukolsky, W. T. Vetterling, and B. P. Flannery, *Numerical Recipes* (Cambridge University Press, Cambridge, 1992).
 - ²¹ S. Hüfner, *Photoelectron Spectroscopy* (Springer, Berlin, 2003).
 - ²² S. Doniach and M. Šunjić, J. Phys. C **3**, 285 (1970).
 - ²³ J. M. Luttinger, Phys. Rev. **119**, 1153 (1960).
 - ²⁴ J. M. Luttinger, Phys. Rev. **121**, 942 (1961).
 - ²⁵ F. B. Anders, N. Grewe, and A. Lorek, Z. Phys. B **83**, 75 (1991).
 - ²⁶ R. W. Helmes, M. Sindel, L. Borda, and J. von Delft, cond-mat/0502329 (2005).
 - ²⁷ R. J. Warburton *et al.*, Nature **405**, 926 (2000).
 - ²⁸ K. Karrai *et al.*, Nature **427**, 135 (2004).
 - ²⁹ J. R. Schrieffer and P. A. Wolff, Phys. Rev. **149**, 491 (1966).
 - ³⁰ K. D. Schotte and U. Schotte, Phys. Rev. **185**, 509 (1969).